Article:
Walkley, B., Ke, X., Provis, J.L. et al. (2021) Activator anion influences the nanostructure of alkali-activated slag cements. The Journal of Physical Chemistry C, 125 (37). pp. 20727-20739. ISSN: 1932-7447

https://doi.org/10.1021/acs.jpcc.1c07328

THE JOURNAL OF PHYSICAL CHEMISTRY C
A JOURNAL OF THE AMERICAN CHEMICAL SOCIETY

pubs.acs.org/JPCC

Article

Activator Anion Influences the Nanostructure of Alkali-Activated Slag Cements

Brant Walkley,* Xinyuan Ke, John L. Provis, and Susan A. Bernal*

Cite This: J. Phys. Chem. C 2021, 125, 20727−20739

Read Online

ACCESS | Metrics & More | Article Recommendations | Supporting Information

ABSTRACT: Alkali-activated materials are promising low-carbon alternatives to Portland cement; however, there remains an absence of a fundamental understanding of the effect of different activator types on their reaction products at the atomic scale. Solid-state ^{27}Al and ^{29}Si magic angle spinning (MAS) nuclear magnetic resonance (NMR) spectroscopy and ^{1}H−^{29}Si cross-polarization MAS NMR spectroscopy are used to reveal the effect of the activator anion on the nanostructure, cross-linking, and local hydration of aged alkali-activated slag cements. The main reaction product identified is a mixed cross-linked/non-cross-linked sodium-substituted calcium aluminosilicate hydrate (C−(N)−A−S−H) gel with a structure comparable to tobermorite 11 Å. Analysis of cross-polarization kinetics revealed that a higher content of soluble silicate in the activator promoted the incorporation of Al into the aluminosilicate chains of C−(N)−A−S−H gels, charge-balanced preferentially by protons within the gel interlayer. In sodium carbonate-activated slag cements, aluminosilicate chains of C−(N)−A−S−H gels are instead charge-balanced preferentially by Ca^{2+} or Al^{V} ions. Hydrotalcite was observed as a secondary reaction product independent of the activator used and in higher quantities as the content of sodium carbonate in the activator increases. The presence of soluble silicates in the activator promotes the formation of an Al-rich sodium aluminosilicate hydrate (N−A−S−H) gel which was not identified when using sodium carbonate as the activator. These results demonstrate that the anion type in the activator promotes significant differences in the nanostructure and local hydration of the main binding phases forming in alkali-activated slag cements. This explains the significant differences in properties identified when using these different activators.

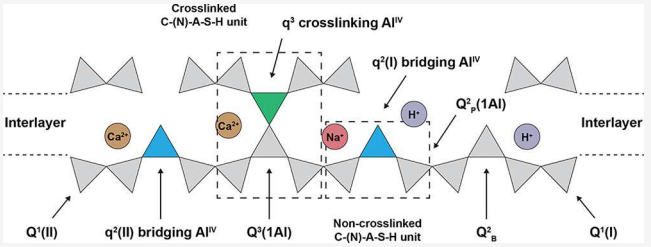

1. INTRODUCTION

Rapidly progressing urbanization has led to an unprecedented rise in the demand for cement and concrete; however, production of Portland cement is associated with the generation of 8% of global anthropogenic CO_2 emissions.[1] This has driven demand for alternative technologies and materials that provide enhanced performance and sustainability. Alkali-activated cements and geopolymers have received significant academic and commercial interest due to their broad technical importance and enhanced sustainability when compared to traditional Portland cements.[2] Modern alkali-activated slag cements exhibit desirable mechanical performance, up to 80% reduction in life cycle CO_2 emissions compared to ordinary Portland cement,[3] and are increasingly applied in the production of concrete.[4,5]

Alkali-activated slag cement is produced by blending ground granulated blast furnace slag with an alkali activator. The predominant reaction product in these cements is a sodium-substituted calcium aluminosilicate hydrate (C−(N)−A−S−H) gel.[6−9] Mg−Al and Ca−Al layered double hydroxides (LDHs) are the commonly formed secondary reaction products,[6−10] together with a small fraction of noncrystalline sodium aluminosilicate hydrate (N−A−S−H) gels.[7,9] The coexistence of these phases within alkali-activated slags results in substantial variation in the phase assemblage, nanostructure, and transport properties which ultimately determine the material performance. In particular, the type and concentration of the alkaline activator have been shown to modify the microstructure and transport properties of alkali-activated slags.[4,6,11−13]

The primary role of the alkaline activators, such as sodium hydroxide (NaOH), sodium silicates ($Na_2O{\cdot}rSiO_2$, where typically $1 \leq r \leq 3$), sodium carbonate (Na_2CO_3), and sodium sulfate (Na_2SO_4), is to generate a high-pH environment which drives the dissolution of the anhydrous precursors and subsequent condensation and precipitation of reaction products. Sodium silicate is in many cases the most effective activator for cements based on conventional blast furnace slags, but the production of sodium silicate-based activators is associated with relatively high cost and CO_2 emissions compared to other potential activators,[14] reducing the economic viability and sustainability of sodium silicate-

Received: August 18, 2021
Revised: August 24, 2021
Published: September 9, 2021

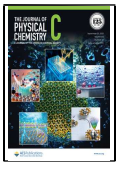

activated slag cements. Recently, sodium carbonate-based activators have received particular attention[12,13,15,16] due to their low cost and enhanced sustainability when compared with sodium silicate-based activators.[17−22] The use of sodium carbonate activators offer great advantages over sodium silicate activation, as the pH of the activating solutions are comparable to those of hydrated Portland cement, and sodium carbonate can be mined or obtained as a byproduct from different chemical processes.[23]

However, there is limited understanding of the nanostructure of the main binding phase formed in sodium carbonate-activated slag cements. Several early studies reported slow reaction, hardening, and strength development,[12,13,16] potentially limiting the application of these materials. Recent studies have demonstrated that these cements can be tailored to react at desirable setting times via the addition of smart inorganic admixtures[24] or by partial replacement of sodium carbonate by sodium silicate.[12] The kinetics of reaction and phase assemblage evolution of sodium carbonate-activated slag cements are strongly dependent on slag chemistry as well as the activation conditions adopted.[7,25] The use of the sodium carbonate activator also enhances the durability performance of these cements against chlorides[21] and significantly improves the CO_2 binding capacity of these cements,[22] without modifying their mechanical performance, compared with sodium silicate-activated slag cements.

Solid-state magic angle spinning nuclear magnetic resonance (MAS NMR) spectroscopy investigations probing ^{27}Al and ^{29}Si nuclei in alkali-activated cementitious materials have proven instrumental in the development of structural models for C−S−H,[26] C−(N)−A−S−H,[27] and N−A−S−H[28] gels. Cross-polarization (CP) MAS NMR is a double-resonance technique[29] which involves transfer of magnetization from an abundant spin system I (e.g., ^{1}H) to a dilute spin system S (e.g., ^{29}Si), allowing acquisition of the NMR spectrum of the dilute spin system S with a much higher signal/noise ratio than would be obtained by single-pulse MAS NMR experiments. Acquisition of CP MAS spectra using an array of Hartmann-Hahn contact times can reveal further information related to the mobility and proximity of the spin systems I and S, to resolve signals from sites exhibiting overlapping resonances in single-pulse spectra. However, this type of analysis has not previously been published for alkali-activated slag cements.

In this study, we use single-pulse ^{27}Al and ^{29}Si MAS NMR and $^{1}H−^{29}Si$ CP MAS NMR experiments, complemented by X-ray diffraction (XRD) measurements, to examine the relationship between the chemical composition of the alkaline activator and the phase assemblage and nanostructure of a series of aged alkali-activated slag cements. Through quantification of the NMR data, spectral deconvolutions, and CP kinetic curves, in line with the structural models of C−(N)−A−S−H, N−A−S−H, and additional reaction products in these systems, we reveal the strong influence of alkali-activator composition on the phase assemblage, nanostructure, and local hydration within aged alkali-activated slags.

2. EXPERIMENTAL METHODS

2.1. Sample Preparation. Alkali-activated slag samples were produced by the reaction of a commercial ground granulated blast furnace slag (Table 1) with either sodium silicate, sodium carbonate, or a combination of sodium silicate and sodium carbonate solutions, to determine the effect of silicate and carbonate anions on the nanostructure of these cements. The three types of alkaline solutions were prepared, as outlined in Table 2.

Table 1. Chemical Composition and Physical Characteristics of Slag Used

component	oxide mass %
SiO_2	33.8
Al_2O_3	13.7
Fe_2O_3	0.4
CaO	42.6
MgO	5.3
Na_2O	<0.1
K_2O	0.4
Others	3.7
loss on ignition	1.8
blaine fineness	410 ± 10 m^2/kg
particle size distribution[a]	0.1−74 μm (d_{50} = 15 μm)

[a]Determined by laser granulometry (Malvern Mastersizer; Malvern Instruments, Malvern, UK).

To produce the carbonate activating solutions, reagent-grade sodium carbonate (Sigma-Aldrich) was fully dissolved in potable water. For the silicate activators, NaOH pellets were dissolved into water and then mixed with a commercial sodium silicate solution (PQ Grade D; SiO_2/Na_2O = 2.0), to achieve a solution of sodium metasilicate composition (Na_2SiO_3), with a SiO_2/Na_2O molar ratio of 1.0. For sample B with a mixed activator, the activating solutions were mixed separately with the anhydrous slag, by first adding the sodium silicate, followed by the sodium carbonate.

Each paste was mixed in a Hobart N50 bench mixer at low speed for 10 min to achieve homogeneity. All paste specimens were cured in sealed centrifuge tubes at 23 °C for 2 years.

2.1.1. X-ray Diffraction. XRD data were obtained across a 2θ range of 5°−55° using a Siemens D5000 instrument with Cu Kα radiation (1.54178 Å), a nickel filter, and a step size of 0.5°/min. Phase identification was performed using JADE XRD software with the ICDD PDF4+ 2015 database.

2.1.2. Solid-State Nuclear Magnetic Resonance Spectroscopy. Solid-state single-pulse ^{27}Al and ^{29}Si MAS NMR spectra were acquired on a Varian VNMRS 400 spectrometer at 9.4 T (B_0), yielding a Larmor frequency of 104.261 MHz for ^{27}Al and 79.495 MHz for ^{29}Si. ^{27}Al MAS NMR spectra were acquired using a 4.0 mm triple resonance probe with zirconia rotors spinning at 14.0 kHz, a 1.0 μs ($\pi/6$) excitation pulse, a 0.2 s relaxation delay, and a total of 7000 scans. ^{29}Si MAS NMR spectra were acquired using a 6.0 mm triple resonance probe with zirconia rotors spinning at 6.8 kHz, a 6.2 μs non-selective ($\pi/2$) excitation pulse, a 5 s relaxation delay, a total of 3000 scans, and a nominal ^{1}H decoupling field strength of 54.3 kHz. $^{1}H−^{29}Si$ CP MAS NMR experiments were performed using the same instrument with a spinning frequency of 6.8 kHz, a ^{29}Si non-selective ($\pi/2$) pulse width of 6.2 μs, an initial ^{1}H non-selective ($\pi/2$) pulse width of 4.5 μs, a recycle delay of 1.0 s, and an array of Hartmann-Hahn contact periods (t = 0.2, 0.4, 3, 5, 10, 15, and 20 ms). A nominal ^{1}H decoupling field strength of 54.3 kHz was employed during acquisition and 16,560 scans were collected per experiment. All ^{27}Al and ^{29}Si spectra were referenced to 1.0 M aqueous $AlCl_3$ and neat tetramethylsilane, respectively, at 0 ppm.

The $^{1}H−^{29}Si$ CP kinetic curves do not show any obvious oscillatory CP kinetics, and therefore, it can be assumed that the proton spin diffusion rate in the samples presented here is

https://doi.org/10.1021/acs.jpcc.1c07328
J. Phys. Chem. C 2021, 125, 20727−20739

Table 2. Activator Chemical Composition, Paste Water-to-Solid Ratio (w/s), and Dosage of Activating Solutions in Each Paste Sample Tested

sample	Activator	Na_2SiO_3:Na_2CO_3 (wt. %)	SiO_2/Na_2O	w/s	dosage (wt %)[a]
A	Na_2SiO_3	100:0	1.0	0.40	8.0
B	Na_2SiO_3 + Na_2CO_3	50:50	0.47	0.40	8.0
C	Na_2CO_3	0:100	0.0	0.40	8.0

[a]Dosage is defined relative to the mass of anhydrous slag.

sufficiently rapid that cross-polarization obeys the classical $I-S$ kinetic theory. CP kinetic curves for the spin system $I-S$ ($^1H-^{29}Si$ in the work presented here) were therefore fitted with a simplified general CP kinetic equation[30] (eq 1) derived from the classical $I-S$ kinetic model, where $I(t)$ is the signal height at contact time t, I_0 is the ideal (full) cross-polarized ^{29}Si magnetization signal intensity (i.e., the extrapolated maximum signal height), T_{HSi} is the CP time constant (which is proportional to the sixth power of the $^1H-^{29}Si$ internuclear distance[31,32]), and $T_{1\rho}^H$ is the proton spin−lattice relaxation time in the rotating frame.

$$I(t) = I_0 \cdot (1 - T_{HSi}/T_{1\rho}^H)^{-1} \cdot [\exp(-t/T_{1\rho}^H) - \exp(-t/T_{HSi})] \quad (1)$$

This simplified version of the general CP kinetic equation is applicable when polarization is transferred from an abundant spin subsystem I (^1H in the work presented here) to a dilute spin subsystem S (^{29}Si in the work presented here) such that the spin population ratio $\varepsilon = N_{Si}/N_H \approx 0$, and the CP rate constant T_{HSi} is much smaller than the relaxation time constant in the rotating frame, $T_{1\rho}^{Si}$, for the dilute spin subsystem S (as is the case for ^{29}Si) such that $T_{HSi}/T_{1\rho}^{Si} \approx 0$. The parameter $1/T_{HSi}$ is often denoted the CP rate constant and is the "rate" at which magnetization is transferred from ^1H to ^{29}Si nuclei.

Gaussian peak profiles were used to deconvolute the ^{29}Si MAS and $^1H-^{29}Si$ CP MAS NMR spectra.[33] The minimum number of peaks possible were fitted, and the chemical shift and peak full width at half-maximum (FWHM) of each resonance were required to be consistent in both the ^{29}Si MAS NMR and $^1H-^{29}Si$ CP MAS NMR spectral deconvolutions. Peak FWHM was restricted to ≤5 ppm for C−(N)−A−S−H gel products and ≤6 ppm for N−A−S−(H) gel products. Peak intensities were required to be consistent with the structural constraints described by the "cross-linked substituted tobermorite model" (CSTM) for C−(N)−A−S−H gel products[27] and the thermodynamics of a statistical distribution of Si and Al sites within a Q^4 aluminosilicate network for N−A−S−(H) gel products.[28] Six resonances were resolved in the $^1H-^{29}Si$ CP MAS NMR spectra and were fitted using Gaussian peak profiles and the constraints discussed above. The ^{29}Si MAS NMR spectra were then fitted with these six resonances plus an additional resonance to account for Si sites in remnant unreacted anhydrous slag. The ^{29}Si MAS NMR spectral deconvolutions were required to be consistent with the constraints discussed above. The ^{27}Al MAS NMR spectra were simulated using DMFit[33,34] and the Czjzek Gaussian isotropic model[35] with the minimum number of peaks to obtain a reasonable fit to the data and determine the isotropic chemical shift, δ_{iso}, for each resonance. Quadrupolar coupling constants, C_Q, were obtained from the literature.[36−38] In all spectral deconvolutions, congruent dissolution of slag was assumed, so a scaled component spectrum was calculated from the ^{29}Si and ^{27}Al MAS NMR spectra of anhydrous slag and used in the fitting.

3. RESULTS AND DISCUSSION

3.1. Mineralogy of Alkali-Activated Slag Cements.

XRD results for each alkali-activated slag sample and the anhydrous slag precursor are shown in Figure 1. The XRD data

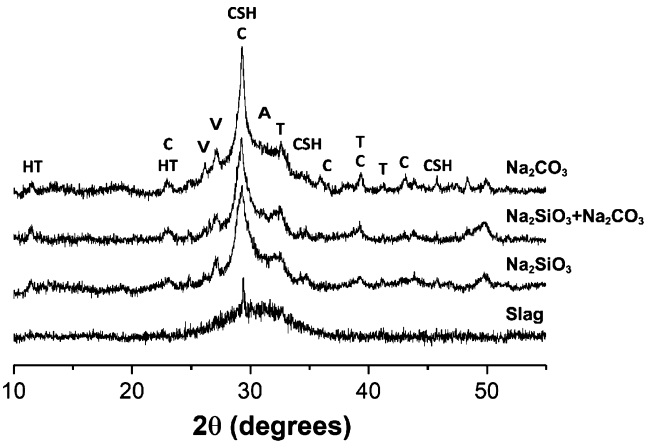

Figure 1. CuK_α diffractograms of anhydrous slag and slag activated with sodium silicate, sodium carbonate, or a combination of sodium silicate and sodium carbonate as marked. CSH: calcium silicate hydrate, HT: hydrotalcite-group LDH phases, T: thermonatrite, C: calcite, V: vaterite, and A: åkermanite.

for anhydrous slag are dominated by a broad diffuse scattering characteristic of its amorphous nature,[9,25] with minor quantities of calcite (powder diffraction file (PDF)# 01-083-0577), vaterite (PDF# 01-074-1867), and åkermanite ($Ca_2MgSi_2O_7$, PDF# 00-035-0592). The XRD data for each alkali-activated slag sample also exhibit a broad feature corresponding to an aluminum-substituted calcium silicate hydrate (C−(A)−S−H) gel that exhibits low crystallinity and some structural similarity to tobermorite-11 Å ($Ca_5(Si_6O_{16})(OH_2)$, PDF# 01-089-6458). Reflections due to Mg-LDH phases in the hydrotalcite group (represented in the PDF database as $Mg_6Al_2(CO_3)(OH)_{16}\cdot 4H_2O$, PDF# 00-041-1428) are also observed in the XRD data for each sample.[6,8] Similar phase assemblages were identified in the same specimens evaluated in this study when cured up to 180 days.[6] This confirms that extending the curing time to 2 years does not induce significant mineralogical changes in alkali-activated slag cements produced either with sodium silicate and/or carbonate solutions.

The Ca-LDH phase described as monocarbonate-AFm ($[Ca_2(Al,Fe)(OH)_6]\cdot CO_3\cdot xH_2O$) has been observed to coexist with hydrotalcite in sodium carbonate-activated slags with similar compositions to those used in this study,[25] in agreement with thermodynamic modeling.[39] However, no clear reflections for this phase are identified in XRD analysis of the aged samples evaluated here.

https://doi.org/10.1021/acs.jpcc.1c07328
J. Phys. Chem. C 2021, 125, 20727−20739

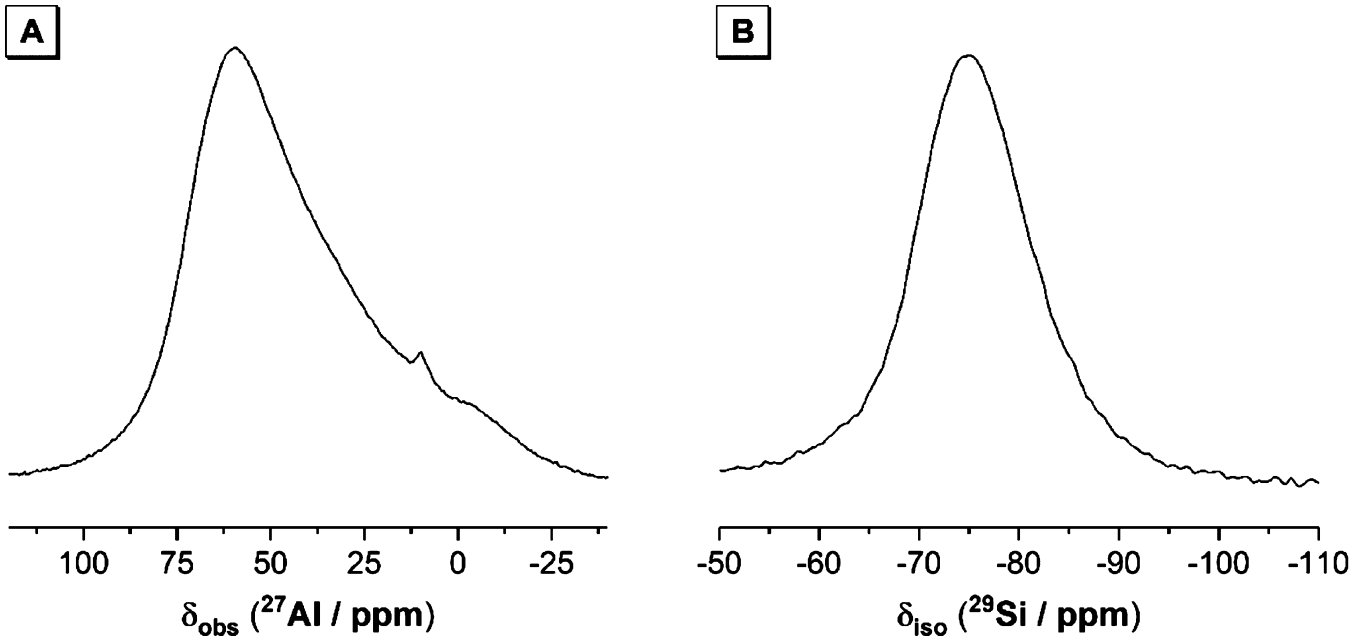

Figure 2. (a) ^{27}Al MAS (B_0 = 9.4 T and ν_R = 14.0 kHz) and (b) ^{29}Si MAS (B_0 = 9.4 T and ν_R = 6.8 kHz) NMR spectra of anhydrous slag.

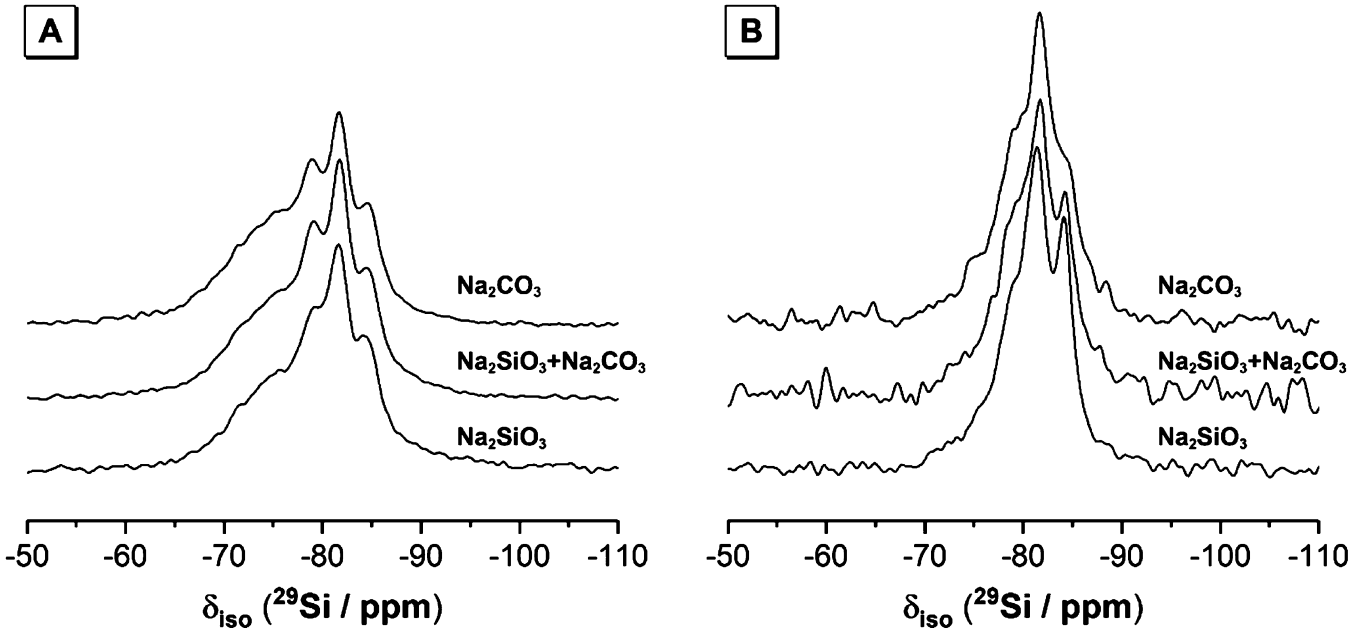

Figure 3. (a) ^{29}Si MAS (B_0 = 9.4 T, ν_R = 6.8 kHz) NMR and (b) ^{1}H−^{29}Si CP MAS (B_0 = 9.4 T, ν_R = 6.8 kHz, Hartmann-Hahn contact period t = 3 ms) NMR spectra of slag activated with sodium silicate, sodium carbonate, or a combination of sodium silicate and sodium carbonate as marked.

Reflections due to polymorphs of calcium carbonate (calcite, PDF# 01-083-0577, and vaterite, PDF# 01-074-1867) and thermonatrite ($Na_2CO_3·H_2O$, PDF# 01-072-0578) were also observed in the XRD data for each alkali-activated slag sample in Figure 1, more prominently than the appearance of the calcium carbonates in the raw slag. The formation of these carbonates in sodium carbonate-activated slag is due to the supply of CO_3^{2-} anions from the activator, while the formation of these phases in sodium silicate-activated samples is attributed to minor weathering of the samples during preparation and analysis.

3.2. Solid-State Nuclear Magnetic Resonance Spectroscopy of Anhydrous Slag. The ^{27}Al MAS NMR data for anhydrous slag (Figure 2a) exhibit a broad tetrahedral Al resonance with the maximum intensity at δ_{obs} = 60 ppm, consistent with the diffuse scattering observed by XRD (Figure 1). This resonance is assigned to a single tetrahedral AlO_4 site, consistent with previous observations using ^{27}Al MAS, ^{27}Al 3Q MAS, and ^{27}Al 5Q MAS NMR.[40] The breadth of this resonance indicates extensive local disorder and asymmetry.[7,41] A sharp, low intensity resonance is also present in the ^{27}Al MAS NMR data at δ_{obs} = 9.8 ppm. This site is tentatively attributed to Al^{VI} in melilite $(Ca, Na)^2(Al, Mg, Fe^{2+})[(Al, Si)SiO_7]$; melilite group minerals form a solid solution between the end members gehlenite ($Ca_2Al_2SiO_7$) and åkermanite ($Ca_2MgSi_2O_7$), the latter of which was observed by XRD as discussed above. This is likely to be a result of some minor weathering of the slag prior to analysis.

https://doi.org/10.1021/acs.jpcc.1c07328
J. Phys. Chem. C 2021, 125, 20727−20739

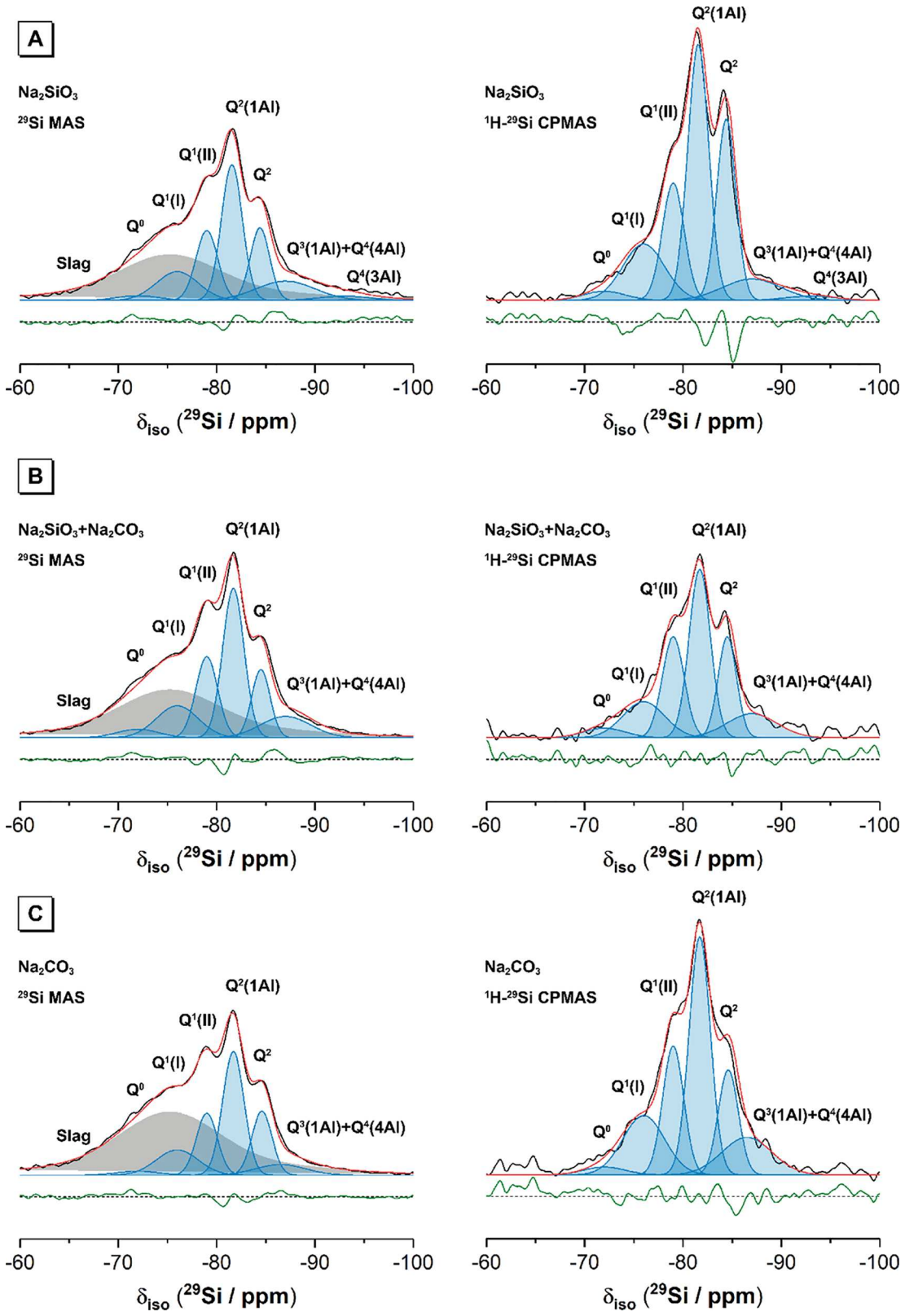

Figure 4. ^{29}Si MAS (B_0 = 9.4 T and ν_R = 6.8 kHz) NMR and (b) ^{1}H−^{29}Si CP MAS (B_0 = 9.4 T, ν_R = 6.8 kHz, and Hartmann-Hahn contact period t = 3 ms) NMR spectra and associated deconvolutions for slag activated with (a) sodium silicate, (b) a combination of sodium silicate and sodium carbonate, and (c) sodium carbonate. All samples are cured for 2 years. In each case, the data are shown in black, the fit (shown in red) is the sum of the deconvoluted peaks, and the difference between the data and the fit is shown in green. Peaks attributed to Si sites in C−(N)−A−S−H are shaded in blue, while those attributed to sites within remnant anhydrous slag are shaded in gray.

The ^{29}Si MAS NMR data for anhydrous slag (Figure 2b) exhibit a single broad resonance with the maximum intensity at δ_{iso} = −75 ppm indicating an extensive distribution of Si environments and chemical shifts, consistent with the poorly

https://doi.org/10.1021/acs.jpcc.1c07328
J. Phys. Chem. C 2021, 125, 20727−20739

Table 3. NMR Parameters Extracted from the Deconvoluted ^{29}Si MAS NMR Spectra for Each Alkali-Activated Slag Sample

		assignment								
Sample	Parameter	unreacted slag	Q^0	Q^1(I)	Q^1(II)	Q^2	Q^2(1Al)	Q^3(1Al)	Q^4(4Al)	Q^4(3Al)
All	δ_{iso} (ppm)[a]		−72	−76	−79	−84.4	−81.6	−87	−87	−93
	FWHM (ppm)[a]		5	5	2.6	2.3	2.5	7	7	6
Na_2SiO_3	relative integral area (%)[b]	40.5	1.4	8.4	10.6	19.9	9.8	7.9	1.5	
Na_2SiO_3 + Na_2CO_3	relative integral area (%)[b]	40.1	2.4	8.9	11.8	21.3	8.4	7.1	0.0	
Na_2CO_3	relative integral area (%)[b]	53.3	1.1	7.1	8.6	17.6	8.6	3.6	0.0	

[a] δ_{iso} is the isotropic chemical shift and FWHM is the full width at half-maximum obtained by simulating the ^{29}Si MAS and ^{1}H−^{29}Si MAS NMR spectra; δ_{iso} and FWHM were required to be consistent in both the ^{29}Si MAS and ^{1}H−^{29}Si MAS NMR spectra. [b] The relative integrated intensity for each resonance is normalized to the sum of all sites within the reaction product and is obtained by simulating the ^{29}Si MAS NMR spectra. Residual slag component contributions were observed in all alkali-activated slag ^{29}Si MAS NMR spectra and are shown in Figure 3 but are excluded from the quantification of C−(N)−A−S−H gel constituents so that the quantification is conducted on the basis of reaction products only. Estimated error in the relative integral area is 1%.

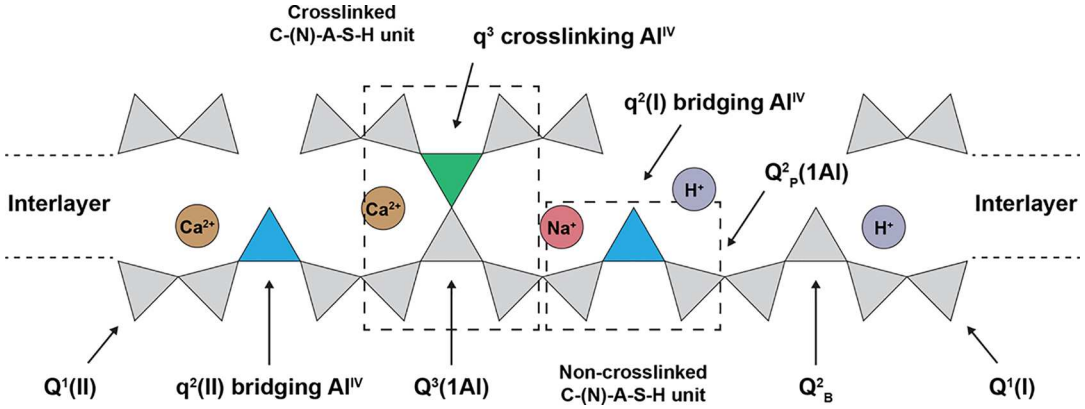

Figure 5. Schematic representation of silicate chains and the interlayer region of C−(N)−A−S−H gels, based on the cross-linked substituted tobermorite model,[27] showing the Si (Q^n(mAl)) and Al (q^n) sites that are identified in spectral deconvolutions of the ^{29}Si MAS NMR, ^{1}H−^{29}Si CP MAS NMR, and ^{27}Al MAS NMR data. Si tetrahedra are shown as gray triangles, while cross-linking and non-cross-linking Al tetrahedra are green and blue, respectively. The calcium hydroxide layers which separate each pair of silicate chains (top and bottom of the graphic as depicted) are omitted for clarity.

crystalline nature of this material, as observed by XRD (Figure 1). This resonance will contain contributions from a distribution of Q^n (mAl) environments (where $0 \le m \le n \le 4$), with the maximum intensity at δ_{iso} = −75 ppm, indicating that this distribution is dominated by species with lower polymerization or higher Al substitution. This is consistent with previous ^{29}Si MAS NMR observations for anhydrous slag.[6,42]

3.3. Nanostructure of Alkali-Activated Slag Cements.

3.3.1. ^{29}Si MAS and ^{1}H−^{29}Si CP MAS NMR Spectroscopy. The ^{29}Si MAS and ^{1}H−^{29}Si CP MAS NMR data (Figure 3) indicate that alkali activation of anhydrous slag with each activating solution results in the formation of reaction products with Si environments resonating at δ_{iso} = −79.0, −81.6, and −84.4 ppm. These resonances are attributed to Q^1, Q^2(1Al), and Q^2 sites within a sodium and aluminum-substituted calcium silicate hydrate (C−(N)−A−S−H) gel[9,43] (Figure 4), consistent with previous observations for sodium silicate- and sodium carbonate-activated slag cements.[9,13] The main difference observed when using sodium silicate and/or carbonate activators is the intensity of a broad feature within the region consistent with the anhydrous slag (Figure 2B), which indicates that different degrees of the reaction are achieved when using different activator types, even at extended curing durations.

The peaks assigned to Q^2(1Al) and Q^2 are more intense when using sodium carbonate as the activator. The intensity of resonances in ^{1}H−^{29}Si CP MAS NMR data is modulated by their proximity to protons and the Hartmann-Hahn contact period (discussed in further detail below), and consequently, this spectrum indicates specifically those Si species that are within the hydrated reaction product. Thus, the ^{1}H−^{29}Si CP MAS NMR data in Figure 3B confirm that the broad feature identified in the ^{29}Si MAS NMR results (Figure 3A) is attributable to the anhydrous slag present in the alkali-activated slag cements, as it is absent from the CP MAS spectra. This enables more detailed analysis of the differences in the nanostructure of C−(N)−A−S−H gels depending on the content of soluble silicates provided to the system upon slag activation.

Deconvolution and quantification of the ^{29}Si MAS and ^{1}H−^{29}Si CP MAS NMR data (Figure 4 and Table 3) highlight the three resonances identified above, as well as the presence of three additional Si environments in each sample, resonating at δ_{iso} = −72.0, −76.0, and −87.0 ppm. All six resonances are unambiguously resolved in the ^{1}H−^{29}Si CP MAS NMR data and can therefore all be attributed to Si sites within the hydrous reaction product. The resonances at δ_{iso} = −72.0, −76.0, and −87.0 ppm are attributed to Q^0, an additional Q^1 site, and a Q^3(1Al) site, respectively, within the C−(N)−A−S−H gel. The identification of the Q^3(1Al) site indicates a significant extent of cross-linking with the C−(N)−A−S−H gel, as illustrated in Figure 5. The identification of two distinct Q^1 sites, hereafter denoted as Q^1(I) and Q^1(II), is consistent

https://doi.org/10.1021/acs.jpcc.1c07328
J. Phys. Chem. C 2021, 125, 20727−20739

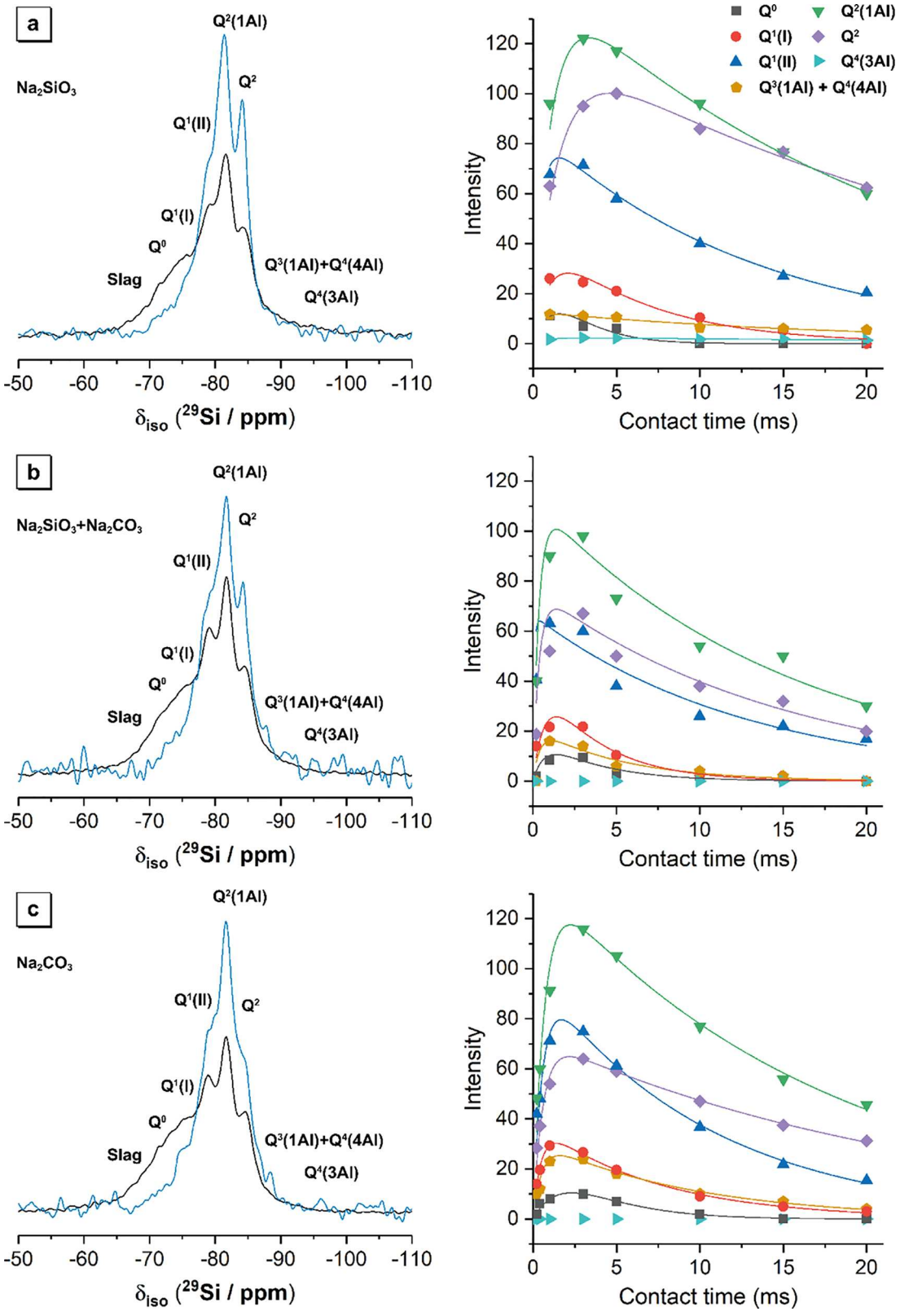

Figure 6. ^{29}Si MAS (B_0 = 9.4 T and ν_R = 6.8 kHz, shown in black) and ^{1}H−^{29}Si CP MAS (B_0 = 9.4 T, ν_R = 6.8 kHz, and Hartmann-Hahn contact period t = 3 ms, shown in blue) NMR spectra, and a comparison of ^{1}H−^{29}Si CP kinetics, for slag activated with (a) sodium silicate, (b) a combination of sodium silicate and sodium carbonate, and (c) sodium carbonate.

with differences in shielding experienced by Q^1 species charge-balanced by Ca^{2+}, Na^+ or H^+, as predicted from molecular dynamics studies[44] and observed in previous ^{29}Si MAS NMR studies of sodium silicate-activated slag.[7] Due to differences in electronegativity, H^+ or Na^+ will shield the Si nuclei to a greater extent than Ca^{2+}, and therefore, the Q^1(I) and Q^1(II) sites are attributed to Q^1 species charge-balanced by Ca^{2+} and by Na^+/H^+, respectively (Figure 4). This assignment is

https://doi.org/10.1021/acs.jpcc.1c07328
J. Phys. Chem. C 2021, 125, 20727−20739

Table 4. NMR Parameters Extracted from the Deconvoluted $^{1}H-^{29}Si$ CP MAS NMR Spectra and CP Kinetic Curves for Each Alkali-Activated Slag Sample

		assignment							
sample	parameter	Q^0	Q^1(I)	Q^1(II)	Q^2	Q^2(1Al)	Q^3(1Al)	Q^4(4Al)	Q^4(3Al)
All	δ_{iso} (ppm)[a]	−72	−76	−79	−84.4	−81.6	−87	−87	−93
	FWHM (ppm)[a]	5	5	2.6	2.3	2.5	7	7	6
Na_2SiO_3	I_0 (arbitrary units)[b]	32.5	39.4	84	117	142	12	12	2.5
	T_{HSi} (ms)[b]	1.6	0.9	0.4	1.4	1.0	0.3	0.3	0.8
	$T^{H}_{1\rho}$ (ms)[b]	1.6	6.2	13.4	30.1	22.2	20.3	20.3	35.5
Na_2SiO_3 + Na_2CO_3	I_0 (arbitrary units)[b]	15	38	66	76	110	20.0		
	T_{HSi} (ms)[b]	0.65	0.7	0.1	0.4	0.4	0.4		
	$T^{H}_{1\rho}$ (ms)[b]	3.62	3.6	13.0	15.1	15.4	5.3		
Na_2CO_3	I_0 (arbitrary units)[b]	23	37	94	71	134	30		
	T_{HSi} (ms)[b]	1.8	0.5	0.5	0.6	0.7	0.5		
	$T^{H}_{1\rho}$ (ms)[b]	2.9	7.3	10.4	23	17.3	9.4		

[a] δ_{iso} is the isotropic chemical shift and FWHM is the full width at half-maximum obtained by simulating the ^{29}Si MAS and $^{1}H-^{29}Si$ MAS NMR spectra; δ_{iso} and FWHM were required to be consistent in both the ^{29}Si MAS and $^{1}H-^{29}Si$ MAS NMR spectra. [b] I_0, T_{HSi}, and $T^{H}_{1\rho}$ are the extrapolated signal intensity, CP time constant, and proton spin−lattice relaxation time in the rotating frame, respectively, and are calculated by fitting the CP kinetic curves with a simplified general CP kinetic equation.[30]

corroborated by T_{HSi} values for each Q^1 site determined by fitting the $^{1}H-^{29}Si$ CP kinetic curves and will be discussed in further detail below.

A significant resonance intensity is also observed at approximately δ_{iso} = −93 ppm in alkali-activated slag cements produced with sodium silicate or sodium silicate/carbonate activating solutions. A resonance with this chemical shift may be assigned to Q^3 and/or Q^4(3Al) environments.[45] However, to maintain consistency with the structural constraints for a mixed cross-linked/non-cross-linked C−(N)−A−S−H gel described by the cross-linked substituted tobermorite model, a separate peak representing Q^4(3Al) resonances at −93 ppm must be fitted.[7,27] This Q^4(3Al) environment is attributed to a polymerized Al-rich (Si/Al ≤ 1.2) N−A−S−H gel that, in the presence of high Al and Na content, has formed in the addition to C−(N)−A−S−H,[7,9,42,46] comprising Q^4(3Al) and Q^4(4Al) Si sites.[28] This resonance is not observed in sodium carbonate-activated slag cements. In cements produced with sodium silicate activators, the resonance at −87 ppm initially attributed to Q^3(1Al) environments will also contain contributions from overlapping resonances from Q^4(4Al) environments. However, it is unlikely that this is the case for sodium carbonate-activated slag cements as there is no other indication of the presence of N−A−S−H gel in these cements.

3.3.1.1. $^{1}H-^{29}Si$ Cross-Polarization Kinetics. A comparison of the ^{29}Si MAS and $^{1}H-^{29}Si$ CP MAS NMR data is shown alongside the $^{1}H-^{29}Si$ CP kinetic curves in Figure 6. Each $^{1}H-^{29}Si$ CP kinetic curve exhibits dynamics characteristic of classical *I*−*S* kinetic theory,[30] with an initial buildup and subsequent decrease in signal intensity with increasing contact time, as described in Section 2.1.2. A simplified general CP kinetic equation[30] derived from the classical *I*−*S* kinetic model was therefore used to determine the ideal cross-polarized signal intensity, I_0, T_{HSi}, and $T^{H}_{1\rho}$ (Table 4).

Magnetization transfer during cross-polarization depends on the strength of the $^{1}H-^{29}Si$ magnetic dipolar interaction; a stronger dipolar interaction will result in faster transfer of magnetization. As the $^{1}H-^{29}Si$ magnetic dipolar interaction (and consequently T_{HSi}) is inversely proportional to both the $^{1}H-^{29}Si$ internuclear distance and the mobility of the surrounding protons,[30] the magnitude of T_{HSi} obtained from fitting the $^{1}H-^{29}Si$ CP kinetic curves can provide information about these physical quantities. Also, as $T^{H}_{1\rho}$ is proportional to the number of surrounding protons, the magnitude of $T^{H}_{1\rho}$ obtained from fitting the $^{1}H-^{29}Si$ CP kinetic curves can provide information regarding the relative number of protons surrounding each site (scaled by the sixth power of the $^{1}H-^{29}Si$ internuclear distance in the case of classical *I*−*S* kinetics) over a distance of approximately 2 nm.[47] This is complicated by the relationship between $T^{H}_{1\rho}$ and the dynamics of the protons, interactions with other spins (including paramagnetic ions), B_0, and the CP experimental conditions, meaning that an element of caution must be used when interpreting this parameter. However, in the work presented here, $T^{H}_{1\rho}$ can provide an indication of the relative number of protons in proximity to Si sites, as the cements analyzed contain very similar phase assemblages and gel structures and were produced from the same precursor materials, and the $^{1}H-^{29}Si$ CP MAS NMR experiments were performed on the same instrument using the same experimental conditions.

Relatively high-quality fits to the CP kinetic curves were obtained for the sodium silicate- and sodium carbonate-activated slag cements; however, lower-quality fits were obtained for slag cements activated with a blend of sodium silicate and sodium carbonate due to the lower signal/noise of the $^{1}H-^{29}Si$ CP MAS NMR spectra for these samples. The buildup in these curves is governed by T_{HSi}, whereas the subsequent decay is influenced primarily by $T^{H}_{1\rho}$. Due to the rapid buildup, there are a limited number of data points in this section of the curve, and the error associated with T_{HSi} is likely to be significantly larger than that for $T^{H}_{1\rho}$. An element of caution should therefore be used when interpreting the fits to the CP kinetic curves, although the general trends observed are informative. Therefore, the data obtained from these fits cannot be interpreted in isolation and must be interpreted within the context of information regarding the local structure of the main binding phases observed in these cements obtained from the ^{29}Si MAS and $^{1}H-^{29}Si$ CP MAS NMR spectral deconvolutions.

In all samples examined here, Q^0 sites exhibit large T_{HSi} values and small $T^{H}_{1\rho}$ values, consistent with these sites being surrounded by a small number of highly mobile protons (which may exist within the $Si(OH)_4$ species themselves as well as nearby molecular water). This suggests that these sites

https://doi.org/10.1021/acs.jpcc.1c07328
J. Phys. Chem. C 2021, 125, 20727−20739

may be structurally similar to those found in strätlingite and mullite, with Si bonded to one or more Al^{VI} sites.[48] All alkali-activated slags exhibit CP parameters such that T_{HSi} (Q^0) ≥ T_{HSi} (Q^1(I)) ≥ T_{HSi} (Q^1(II)) and $T^H_{1\rho}$ (Q^0) ≤ $T^H_{1\rho}$ (Q^1(I)) ≤ $T^H_{1\rho}$ (Q^1(II)), suggesting a shorter $^1H-^{29}Si$ internuclear distance and lower proton mobility for Q^1 sites compared with Q^0 ($Si(OH)_4$). In all samples, Q^1(I) exhibits a larger T_{HSi} value than Q^1(II), suggesting faster cross-polarization and a shorter $^1H-^{29}Si$ internuclear distance of Q^1(II) species. This is consistent with the assignment of the Q^1(I) and Q^1(II) peaks to Q^1 sites charge-balanced by Ca^{2+} and by Na^+/H^+, respectively, as identified by differences in δ_{iso} for these sites (Figure 4) and discussed above.

T_{HSi} values for Q^2 sites are generally shorter than those for Q^1 sites in all samples, and Q^2 sites also have longer $T^H_{1\rho}$ values than Q^1 sites (seen by the slower decay of the $^1H-^{29}Si$ CP kinetic curves for these sites in Figure 6), suggesting that Q^2 sites have a longer $^1H-^{29}Si$ internuclear distance and that there are fewer protons surrounding these Q^2 sites relative to Q^1 sites. In slags activated with sodium silicate or sodium carbonate, Q^2(1Al) sites exhibit shorter $T^H_{1\rho}$ values than Q^2 sites, while T_{HSi} values for Q^2(1Al) and Q^2 sites are approximately equal. This suggests a greater number of mobile protons nearby Q^2(1Al) sites than Q^2 sites. In slags activated with blended sodium silicate and carbonate, the T_{HSi} and $T^H_{1\rho}$ values for Q^2(1Al) and Q^2 sites are similar, suggesting a similar association of protons with these two sites.

In all samples, the resonance in the ^{29}Si MAS and $^1H-^{29}Si$ CP MAS NMR data that contain contributions from Q^3(1Al) and Q^4(4Al) sites exhibits small T_{HSi} values and large $T^H_{1\rho}$ values, consistent with close association of these sites with a smaller number of protons that have low mobility. This aligns well with the increased structural rigidity expected for these sites within C−(N)−A−S−H[27] and N−A−S−H gels.[28] The smallest T_{HSi} value and the largest $T^H_{1\rho}$ value are exhibited by this resonance in the sodium silicate-activated slag, consistent with previous observations of greater cross-linking (and hence greater structural rigidity) in slags activated with sodium silicate compared with other activators.[15,16] The Q^4(3Al) site observed in the ^{29}Si MAS and $^1H-^{29}Si$ CP MAS NMR data for sodium silicate-activated slag exhibits a much larger $T^H_{1\rho}$ value (35.5 ms) than all other sites in all samples and a very small T_{HSi} value (0.8 ms). This indicates that this site possesses the largest $^1H-^{29}Si$ internuclear distance and is therefore associated with the smallest number of protons, which are very rigid. This aligns with the greater structural rigidity of the three-dimensional N−A−S−H gel framework than the chains of C−(N)−A−S−H gels and the fact that there are no −OH groups in the immediate vicinity of a Q^4-type site.

3.3.1.2. ^{27}Al MAS NMR Spectroscopy. The ^{27}Al MAS NMR spectra for each alkali-activated sample (Figure 7) exhibit a broad tetrahedral Al resonance spanning from δ_{obs} = 80 to 50 ppm, a broad pentahedral Al resonance centered at δ_{obs} = 37 ppm, and a broad octahedral Al resonance spanning from δ_{obs} = 20 to 0 ppm. Both the tetrahedral and octahedral Al resonances clearly contain contributions from multiple Al sites. This is confirmed by the extensive quadrupolar broadening occurring at B_0 = 9.4 T, so only significantly ordered sites will exhibit a quadrupolar lineshape (c.f. ^{27}Al MAS NMR spectra (B_0 = 9.4 T) of CA, CA_3, C_3A, ettringite, and monosulfate[49]); however, the XRD data for the cements studied here (Figure 1) showed the absence of any significant quantity of Al-containing crystalline phases. The ratio of the intensity of each

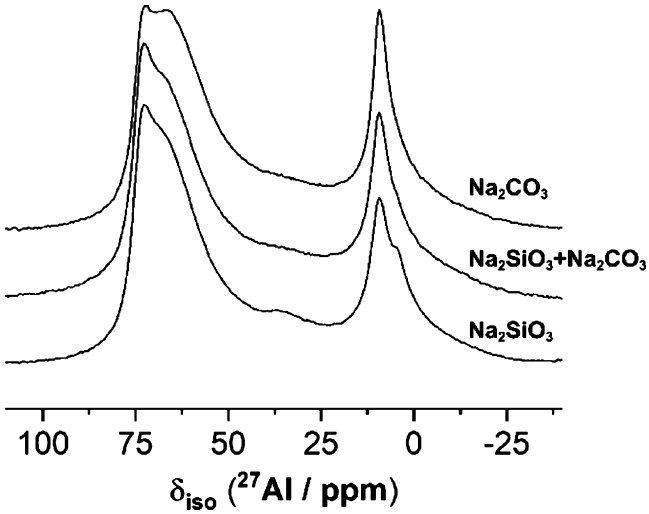

Figure 7. ^{27}Al MAS (B_0 = 9.4 T and ν_R = 14 kHz) NMR spectra of slag activated with sodium silicate, sodium carbonate, or a combination of sodium silicate and sodium carbonate as marked.

of the overlapping sites varies between samples (for both tetrahedral and octahedral sites), which would not be observed for a single site exhibiting a quadrupolar lineshape.[49] Deconvolution and simulation of the ^{27}Al MAS NMR data (Figure 8 and Table 5) resolve three distinct tetrahedral Al sites at δ_{iso} = 74.0, 68.4, and 72.0 ppm. The resonances at δ_{iso} = 68.4 and 72.0 ppm are attributed to Al in bridging tetrahedra (q^2(II))[50,51] and Al in cross-linked bridging tetrahedra (q^3)[7,15,16] (Figure 5) within the aluminosilicate chains in the C−(N)−A−S−H gels, respectively.[9,13,52] Similar amounts of q^2(II) and q^3 sites are formed in each sample.

The resonance at δ_{iso} = 74.0 (q^2(I)) is attributed to Al in a q^2 site distinct from q^2(II), which may possibly result from differences in the local coordination spheres of q^2 bridging sites due to clustering of different charge-balancing cations (as observed in the ^{29}Si MAS and $^1H-^{29}Si$ CP MAS NMR data discussed above), or which may possibly result from the presence of Al in pairing tetrahedra, q^2(P), as observed previously.[50,53] The observation of q^2(P) sites contrasts with the standard interpretation of the C−A−S−H structure, which excludes Al from substituting for Si in pairing tetrahedra[27,43] as there is a strong thermodynamic preference of Al substitution into bridging tetrahedra within the C−A−S−H gel[54] and tobermorite.[51] The large intensity of the q^2(I) resonance in the ^{27}Al MAS NMR data for all samples would suggest that this resonance therefore arises due to Al in a q^2 bridging site charge-balanced by Ca^{2+} ions, which consequently experiences a lower electron density than the Al in bridging sites charge-balanced by Na^+ or H^+ ions (Figure 5). A similar amount of q^2(I) sites are formed in each sample.

The peak FWHM of q^2(I) (6.5 ppm) is slightly less than that of q^2(II) (7.5 ppm), while the C_Q of q^2(I) (1.1 MHz) is much lower that of q^2(II) (2.0 MHz). This indicates less disorder of the C−(N)−A−S−H aluminosilicate chains and less perturbation of the local electric field gradient (EFG) surrounding q^2(I) sites compared to q^2(II) sites, consistent with their assignments here. The presence of q^3 sites exhibiting a significant degree of asymmetry and perturbation of the local EFG (C_Q = 3.0 MHz) indicates a significant level of aluminosilicate chain cross-linking in the C−(N)−A−S−H gel, aligning with previous observations for silicate-activated

https://doi.org/10.1021/acs.jpcc.1c07328
J. Phys. Chem. C 2021, 125, 20727−20739

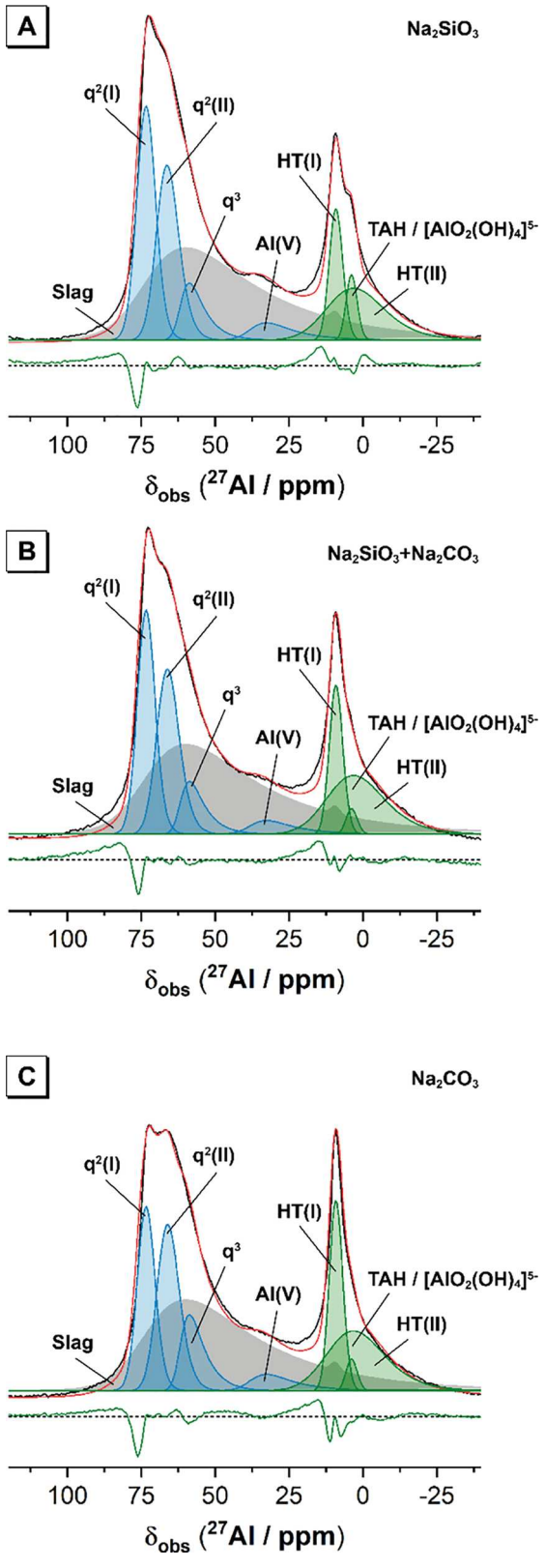

Figure 8. ^{27}Al MAS (B_0 = 9.4 T and ν_R = 14 kHz) NMR spectra and associated deconvolutions for slag activated with (a) sodium silicate, (b) a combination of sodium silicate and sodium carbonate, and (c) sodium carbonate. All samples are cured for 2 years. In each case, the data are shown in black, the fit (shown in red) is the sum of the deconvoluted peaks, and the difference between the data and the fit is shown in green. Peaks attributed to Si sites in C−(N)−A−S−H are shown in blue, peaks attributed to additional reaction products (i.e., hydrotalcite and TAH/$[AlO_2(OH)_4]^{5-}$) are shown in green, and peaks attributed to sites within remnant anhydrous slag are shown shaded in gray, with the simulated spectrum of anhydrous slag also shown in Figure S1 of Supporting Information.

slags.[7,15,16] In all samples, a broad resonance from remnant anhydrous slag particles is also observed.

A single Al^V (δ_{iso} = 38.0 ppm, C_Q = 4.0 MHz) environment is identified in the ^{27}Al MAS NMR data for all samples and is attributed to charge-balancing Al^V within C−(N)−A−S−H gel interlayers.[7] While the existence of five-coordinated Al within the C−(N)−A−S−H gel interlayer has been hypothesized,[36,52,55] it is not included in current structural descriptions of C−(N)−A−S−H gels.[27] However, the observation of a new ^{27}Al MAS NMR resonance due to an Al^V environment whose intensity cannot be attributed solely to remnant anhydrous slag particles is unambiguous in the data presented here, and this has also recently been observed by ^{27}Al multiple quantum MAS NMR analysis of synthetic C−(N)−A−S−H gels.[53]

The number of charge-balancing Al^V atoms within the C−(N)−A−S−H gel interlayers (determined by the relative integral area of the resonance attributed to this peak) decreases significantly with increasing activator SiO_3^{2-} content. This is possibly due to the increased substitution of Al for Si in the aluminosilicate chains in C−(N)−A−S−H in samples produced with higher activator SiO_3^{2-} content and the consequent reduction of excess Al species that may be available to participate in charge-balancing.

Two Al^{VI} environments attributed to Al in a hydrotalcite-type LDH reaction product are identified in the ^{27}Al MAS NMR data for all samples,[7,38,56] consistent with the XRD data presented above. The resonances due to these environments appear at δ_{iso} = 10.0 ppm (HT(I)) and δ_{iso} = 9.42 ppm (HT(II)), with C_Q values of 2.3 and 3.55 MHz, respectively, and are attributed, respectively, to Al^{VI} coordinated to both OH^- and CO_3^{2-} anions ((HT(I))) and Al^{VI} coordinated solely to CO_3^{2-} anions (HT(II)).[38] The sum of the intensity of the HT(I) and HT(II) resonances, and hence the amount of hydrotalcite in the sample, increases with increasing activator CO_3^{2-} content, as one would expect from simple stoichiometric arguments.

A resonance at δ_{iso} = 4.60 ppm (C_Q = 1.13 MHz) is also resolved in the deconvoluted ^{27}Al MAS NMR spectra for all samples. Until recently, this resonance has typically been attributed to the "third aluminate hydrate" (TAH), thought to be an amorphous nanoscale aluminate hydrate phase precipitated at the surface of the C-(N)-A-S-H gels within alkali-activated slags and other calcium-rich binders.[7,9,36,57,58] However, recent work using one- and two-dimensional dynamic nuclear polarization-enhanced ^{27}Al and ^{29}Si MAS NMR experiments attributed this resonance to silicate-bridging $[AlO_2(OH)_4]^{5-}$ sites in C−A−S−H[59] and postulated that TAH does not exist. The attribution of this resonance in that study was based on atomistic simulations, and therefore, it could still reflect an amorphous aluminate phase on the C−A−S−H surface, interacting with nearby Q^1 silicate sites. The intensity of this resonance in the work here is similar across all samples, indicating the formation of a similar amount of this site in each case and suggesting that its formation is not influenced by differences in activator SiO_3^{2-} or CO_3^{2-} content.

https://doi.org/10.1021/acs.jpcc.1c07328
J. Phys. Chem. C 2021, 125, 20727−20739

Table 5. NMR Parameters Extracted from the Deconvoluted ^{27}Al MAS NMR Spectra for Each Alkali-Activated Slag Sample[a,b]

Phase	assignment	coordination	δ_{iso} (ppm)	FWHM (ppm)	C_Q (MHz)	relative integral area (%)		
						Na_2SiO_3	Na_2SiO_3 + Na_2CO_3	Na_2CO_3
Slag	Al(IV)	Al(IV)	74	19.0	6.7	41.4	41.8	41.0
	Al(VI)	Al(VI)	10	3.0	1.0	16.1	15.1	12.0
C−(N)−A−S−H	q^2(I)	Al(IV)	74	6.5	1.1	14.3	14.1	13.7
	q^2(II)	Al(IV)	68.4	7.5	2.0	5.1	4.9	6.9
	q^3	Al(IV)	62.0	5.0	3.0	2.9	2.4	2.8
	Al(V)	Al(V)	38.0	8.0	4.0	6.4	7.5	9.3
Hydrotalcite	HT(I)	Al(VI)	10.0	5.0	1.20	11.1	13.0	12.9
	HT(II)	Al(VI)	9.42	18	3.55	2.6	1.0	1.3
TAH/$[AlO_2(OH)_4]^{5-}$	TAH	Al(VI)	4.6	4	1.13	0.2	0.2	0.2

[a] δ_{iso} is the isotropic chemical shift; FWHM is the full width at half-maximum obtained by simulating the ^{27}Al MAS NMR spectrum; and C_Q is the quadrupolar coupling constant and was obtained from the literature.[36−38] [b] The relative integrated intensity for each resonance is normalized to the sum of all sites within the sample; estimated error in the relative integral area is 1%.

4. CONCLUSIONS

Through the application of multinuclear spectroscopic and diffractometric analysis of alkali-activated slag cements, new insights have been revealed into the nanostructure and local hydration of the gels that are formed in these materials, as a function of the anion type supplied by the activator used. In the activated slag cements assessed, the main reaction product is a mixed cross-linked/non-cross-linked C−(N)−A−S−H gel exhibiting a structure similar to tobermorite 11 Å. In alkali-activated slag cements produced with sodium silicate or sodium silicate/carbonate activators, an Al-rich N−A−S−H gel exhibiting a three-dimensional framework structure is also identified as a reaction product. This gel is not observed in sodium carbonate-activated slag cements. A Mg-rich LDH in the hydrotalcite group and an Al^{VI} site in either the "TAH" or silicate-bridging $[AlO_2(OH)_4]^{5-}$ sites in C−(N)−A−S−H are observed in all the cements assessed, and the amounts of these phases do not seem to be strongly influenced by the content of silicate in the activator. Al atoms within the C−(N)−A−S−H gel substitute for Si^{IV} in q^3 cross-linking and q^2 bridging sites, and charge-balancing Al^V is also present within C−(N)−A−S−H gel interlayers.

The presence of q^3 sites exhibiting a significant degree of asymmetry and perturbation of the local EFG indicates a significant level of aluminosilicate chain cross-linking in the C−(N)−A−S−H gel in aged alkali-activated slag samples. Similar amounts of q^2(I), q^2(II), and q^3 sites are formed in each sample; however, the number of charge-balancing Al^V atoms within the C−(N)−A−S−H gel interlayers decreases with increasing activator SiO_3^{2-} content.

As the activator SiO_3^{2-} content is increased, Q^2(1Al) sites within the alkali-activated slags become more closely associated with protons, while Q^2(0Al) sites exhibit a similar association with protons in slags activated with both silicate- and carbonate-based solutions. Al atoms that have substituted for Si atoms within Q^2 sites in the aluminosilicate chains of C−(N)−A−S−H gels formed in sodium silicate-activated slags are therefore charge-balanced preferentially by protons within the gel interlayer, while those in the aluminosilicate chains of C−(N)−A−S−H gels formed in sodium carbonate-activated slags are charge-balanced preferentially by Ca^{2+} or Al^{IV} ions. Increasing activator SiO_3^{2-} content also leads to clustering of charge-balancing protons around Q^2(1Al) sites in the Al-rich C−(N)−A−S−H gels.

While this study has revealed new insights into the nanostructure and local hydration of the gels that are formed in sodium silicate- and sodium carbonate-activated slag cements, there remain a number of limitations of the current work, primarily in relation to interpretation of the ^{1}H−^{29}Si CP MAS NMR data. As discussed in the main text, the relationship between $T_{1\rho}^H$ and the dynamics of the protons, interactions with other spins (including paramagnetic ions), B_0, and the CP experimental conditions are particularly complicated. This means that an element of caution must be used when interpreting $T_{1\rho}^H$. In the work presented here, $T_{1\rho}^H$ can provide an indication of the relative number of protons in proximity to Si sites, as the cements analyzed contain very similar phase assemblages and gel structures and were produced from the same precursor materials, and the ^{1}H−^{29}Si CP MAS NMR experiments were performed on the same instrument using the same experimental conditions.

Relatively high-quality fits to the CP kinetic curves were obtained for the sodium silicate- and sodium carbonate-activated slag cements; however, lower-quality fits were obtained for slag cements activated with a blend of sodium silicate and sodium carbonate due to the lower signal/noise of the ^{1}H−^{29}Si CP MAS NMR spectra for these samples. The buildup in these curves is governed by T_{HSi}, whereas the subsequent decay is influenced primarily by $T_{1\rho}^H$.

The error associated with T_{HSi} is also likely to be significantly larger than that for $T_{1\rho}^H$, for slag cements activated with a blend of sodium silicate and sodium carbonate, due to a rapid buildup, consequent limited number of data points in this section of the curve, and the lower signal/noise of the ^{1}H−^{29}Si CP MAS NMR spectra for these samples. The data obtained from these fits should therefore not be interpreted in isolation and must be interpreted within the context of information regarding the local structure of the main binding phases observed in these cements obtained from the ^{29}Si MAS and ^{1}H−^{29}Si CP MAS NMR spectral deconvolutions.

■ ASSOCIATED CONTENT

Supporting Information

The Supporting Information is available free of charge at https://pubs.acs.org/doi/10.1021/acs.jpcc.1c07328.

Additional figure showing ^{29}Si MAS NMR data and associated deconvolution for anhydrous slag, as discussed in the main text (PDF)

https://doi.org/10.1021/acs.jpcc.1c07328
J. Phys. Chem. C 2021, 125, 20727−20739

AUTHOR INFORMATION

Corresponding Authors

Brant Walkley − *Department of Chemical and Biological Engineering and Department of Materials Science and Engineering, The University of Sheffield, Sheffield S1 3JD, U.K.;* orcid.org/0000-0003-1069-1362; Email: b.walkley@sheffield.ac.uk

Susan A. Bernal − *School of Civil Engineering, University of Leeds, Leeds LS2 9JT, U.K.; Department of Materials Science and Engineering, The University of Sheffield, Sheffield S1 3JD, U.K.;* Email: s.a.bernallopez@leeds.ac.uk

Authors

Xinyuan Ke − *Department of Architecture and Civil Engineering, University of Bath, Bath BA2 7AY, U.K.; Department of Materials Science and Engineering, The University of Sheffield, Sheffield S1 3JD, U.K.*

John L. Provis − *Department of Materials Science and Engineering, The University of Sheffield, Sheffield S1 3JD, U.K.;* orcid.org/0000-0003-3372-8922

Complete contact information is available at: https://pubs.acs.org/10.1021/acs.jpcc.1c07328

Notes

The authors declare no competing financial interest.

ACKNOWLEDGMENTS

This study has been funded by the Engineering and Physical Sciences Research Council (EPSRC), UK, through grant EP/M003272/1. Participation of S.A. Bernal was partially funded by the EPSRC through EC fellowship EP/R001642/1. All solid-state NMR spectra were obtained at the EPSRC UK National Solid-state NMR Service at Durham, and we thank Dr David Apperley for his assistance with acquiring the data. We also thank the anonymous reviewers of an earlier version of this article for their constructive input regarding interpretation of some of the NMR data.

REFERENCES

(1) Olivier, J. G. J.; Janssens-Maenhout, G.; Peters, J. A. H. W. *Trends in Global CO_2 Emissions; 2012 Report*; PBL Netherlands Environmental Assessment Agency: The Hague, Netherlands, 2012.

(2) Provis, J. L.; van Deventer, J. S. J. *Alkali Activated Materials. State-of-the-Art Report, RILEM TC 224-AAM*; Springer: Dordrecht, 2014; Vol. *13*.

(3) Habert, G.; Ouellet-Plamondon, C. Recent Update on the Environmental Impact of Geopolymers. *RILEM Tech. Lett.* **2016**, *1*, 17−23.

(4) Juenger, M. C. G.; Winnefeld, F.; Provis, J. L.; Ideker, J. H. Advances in Alternative Cementitious Binders. *Cem. Concr. Res.* **2011**, *41*, 1232−1243.

(5) Bernal, S. A.; Provis, J. L. Durability of Alkali-Activated Materials: Progress and Perspectives. *J. Am. Ceram. Soc.* **2014**, *97*, 997−1008.

(6) Bernal, S. A.; San Nicolas, R.; Myers, R. J.; Mejía de Gutiérrez, R.; Puertas, F.; van Deventer, J. S. J.; Provis, J. L. MgO Content of Slag Controls Phase Evolution and Structural Changes Induced by Accelerated Carbonation in Alkali-Activated Binders. *Cem. Concr. Res.* **2014**, *57*, 33−43.

(7) Myers, R. J.; Bernal, S. A.; Gehman, J. D.; van Deventer, J. S. J.; Provis, J. L. The Role of Al in Cross-Linking of Alkali-Activated Slag Cements. *J. Am. Ceram. Soc.* **2015**, *98*, 996−1004.

(8) Haha, M. B.; Lothenbach, B.; Le Saoût, G.; Winnefeld, F. Influence of Slag Chemistry on the Hydration of Alkali-Activated Blast-Furnace Slag—Part I: Effect of Mgo. *Cem. Concr. Res.* **2011**, *41*, 955−963.

(9) Bernal, S. A.; Provis, J. L.; Walkley, B.; San Nicolas, R.; Gehman, J. D.; Brice, D. G.; Kilcullen, A. R.; Duxson, P.; van Deventer, J. S. J. Gel Nanostructure in Alkali-Activated Binders Based on Slag and Fly Ash, and Effects of Accelerated Carbonation. *Cem. Concr. Res.* **2013**, *53*, 127−144.

(10) Walkley, B.; San Nicolas, R.; Sani, M.-A.; Bernal, S. A.; van Deventer, J. S. J.; Provis, J. L. Structural Evolution of Synthetic Alkali-Activated CaO-MgO-Na_2O-Al_2O_3-SiO_2 Materials Is Influenced by Mg Content. *Cem. Concr. Res.* **2017**, *99*, 155−171.

(11) Wang, S.-D.; Pu, X.-C.; Scrivener, K. L.; Pratt, P. L. Alkali-Activated Slag Cement and Concrete: A Review of Properties and Problems. *Adv. Cem. Res.* **1995**, *7*, 93−102.

(12) Bernal, S. A.; San Nicolas, R.; van Deventer, J. S. J.; Provis, J. L. Alkali-Activated Slag Cements Produced with a Blended Sodium Carbonate/Sodium Silicate Activator. *Adv. Cem. Res.* **2016**, *28*, 262−273.

(13) Bernal, S. A.; Provis, J. L.; Myers, R. J.; San Nicolas, R.; van Deventer, J. S. J. Role of Carbonates in the Chemical Evolution of Sodium Carbonate-Activated Slag Binders. *Mater. Struct* **2015**, *48*, 517−529.

(14) Fawer, M.; Concannon, M.; Rieber, W. Life Cycle Inventories for the Production of Sodium Silicates. *Int. J. Life Cycle Assess.* **1999**, *4*, 207.

(15) Palacios, M.; Puertas, F. Effect of Carbonation on Alkali-Activated Slag Paste. *J. Am. Ceram. Soc.* **2006**, *89*, 3211−3221.

(16) Fernández-Jiménez, A.; Puertas, F.; Sobrados, I.; Sanz, J. Structure of Calcium Silicate Hydrates Formed in Alkaline-Activated Slag: Influence of the Type of Alkaline Activator. *J. Am. Ceram. Soc.* **2003**, *86*, 1389−1394.

(17) Bai, Y.; Collier, N. C.; Milestone, N. B.; Yang, C. H. The Potential for Using Slags Activated with near Neutral Salts as Immobilisation Matrices for Nuclear Wastes Containing Reactive Metals. *J. Nucl. Mater.* **2011**, *413*, 183−192.

(18) Sakulich, A. R.; Miller, S.; Barsoum, M. W. Chemical and Microstructural Characterization of 20-Month-Old Alkali-Activated Slag Cements. *J. Am. Ceram. Soc.* **2010**, *93*, 1741−1748.

(19) Provis, J. L.; Duxson, P.; Kavalerova, E.; Krivenko, P. V.; Pan, Z.; Puertas, F.; van Deventer, J. S. J. Historical Aspects and Overview. In *Alkali Activated Materials: State-of-the-Art Report, RILEM TC 224-AAM*; Provis, J. L., van Deventer, J. S. J., Eds.; Springer Netherlands: Dordrecht, 2014; pp 11−57.

(20) Provis, J. L.; Brice, D. G.; Buchwald, A.; Duxson, P.; Kavalerova, E.; Krivenko, P. V.; Shi, C.; van Deventer, J. S. J.; Wiercx, J. A. L. M. Demonstration Projects and Applications in Building and Civil Infrastructure. In *Alkali Activated Materials: State-of-the-Art Report, RILEM TC 224-AAM*; Provis, J. L., van Deventer, J. S. J., Eds.; Springer Netherlands: Dordrecht, 2014; pp 309−338.

(21) Ke, X.; Bernal, S. A.; Hussein, O. H.; Provis, J. L. Chloride Binding and Mobility in Sodium Carbonate-Activated Slag Pastes and Mortars. *Mater. Struct* **2017**, *50*, 252.

(22) Ke, X.; Criado, M.; Provis, J. L.; Bernal, S. A. Slag-Based Cements That Resist Damage Induced by Carbon Dioxide. *ACS Sustainable Chem. Eng.* **2018**, *6*, 5067−5075.

(23) Bernal, S. A. Advances in Near-Neutral Salts Activation of Blast Furnace Slags. *RILEM Tech. Lett.* **2016**, *1*, 39−44.

(24) Ke, X.; Bernal, S. A.; Provis, J. L. Uptake of Chloride and Carbonate by Mg-Al and Ca-Al Layered Double Hydroxides in Simulated Pore Solutions of Alkali-Activated Slag Cement. *Cem. Concr. Res.* **2017**, *100*, 1−13.

(25) Ke, X.; Bernal, S. A.; Provis, J. L. Controlling the Reaction Kinetics of Sodium Carbonate-Activated Slag Cements Using Calcined Layered Double Hydroxides. *Cem. Concr. Res.* **2016**, *81*, 24−37.

(26) Richardson, I. G.; Groves, G. W. The Incorporation of Minor and Trace Elements into Calcium Silicate Hydrates (C-S-H) Gel in Hardened Cement Pastes. *Cem. Concr. Res.* **1993**, *23*, 131−138.

(27) Myers, R. J.; Bernal, S. A.; San Nicolas, R.; Provis, J. L. Generalized Structural Description of Calcium-Sodium Aluminosilicate Hydrate Gels: The Cross-Linked Substituted Tobermorite Model. *Langmuir* **2013**, *29*, 5294−5306.
(28) Provis, J. L.; Duxson, P.; Lukey, G. C.; van Deventer, J. S. J. Statistical Thermodynamic Model for Si/Al Ordering in Amorphous Aluminosilicates. *Chem. Mater.* **2005**, *17*, 2976−2986.
(29) Pines, A.; Gibby, M. G.; Waugh, J. S. Proton-Enhanced NMR of Dilute Spins in Solids. *J. Chem. Phys.* **1973**, *59*, 569−590.
(30) Kolodziejski, W.; Klinowski, J. Kinetics of Cross-Polarization in Solid-State NMR: A Guide for Chemists. *Chem. Rev.* **2002**, *102*, 613−628.
(31) Klein Douwel, C. H.; Maas, W. E. J. R.; Veeman, W. S.; Werumeus Buning, G. H.; Vankan, J. M. J. Miscibility in PMMA/PVF_2 Blends, Studied by ^{19}F-^{13}C CPMAS NMR. *Macromolecules* **1990**, *23*, 406−412.
(32) Eijkelenboom, A. P. A. M.; Maas, W. E. J. R.; Veeman, W. S.; Buning, G. H. W.; Vankan, J. M. J. Triple-Resonance ^{19}F, 1H, Carbon-^{13}C CP-MAS NMR Study of the Influence of PMMA Tacticity on the Miscibility in PMMA/PVF2 Blends. *Macromolecules* **1992**, *25*, 4511−4518.
(33) Massiot, D.; Fayon, F.; Capron, M.; King, I.; Le Calvé, S.; Alonso, B.; Durand, J.-O.; Bujoli, B.; Gan, Z.; Hoatson, G. Modelling One- and Two-Dimensional Solid-State NMR Spectra. *Magn. Reson. Chem.* **2002**, *40*, 70−76.
(34) Neuville, D. R.; Cormier, L.; Massiot, D. Al Environment in Tectosilicate and Peraluminous Glasses: A ^{27}Al MQ-MAS NMR, Raman, and XANES Investigation. *Geochim. Cosmochim. Acta* **2004**, *68*, 5071−5079.
(35) d'Espinose de Lacaillerie, J.-B.; Fretigny, C.; Massiot, D. MAS NMR Spectra of Quadrupolar Nuclei in Disordered Solids: The Czjzek Model. *J. Magn. Reson.* **2008**, *192*, 244−251.
(36) Andersen, M. D.; Jakobsen, H. J.; Skibsted, J. A New Aluminium-Hydrate Species in Hydrated Portland Cements Characterized by ^{27}Al and ^{29}Si MAS NMR Spectroscopy. *Cem. Concr. Res.* **2006**, *36*, 3−17.
(37) Engelhardt, G.; Koller, H. A Simple Procedure for the Determination of the Quadrupole Interaction Parameters and Isotropic Chemical Shifts from Magic Angle Spinning NMR Spectra of Half-Integer Spin Nuclei in Solids. *Magn. Reson. Chem.* **1991**, *29*, 941−945.
(38) Sideris, P. J.; Blanc, F.; Gan, Z.; Grey, C. P. Identification of Cation Clustering in Mg−Al Layered Double Hydroxides Using Multinuclear Solid State Nuclear Magnetic Resonance Spectroscopy. *Chem. Mater.* **2012**, *24*, 2449−2461.
(39) Myers, R. J.; Lothenbach, B.; Bernal, S. A.; Provis, J. L. Thermodynamic Modelling of Alkali-Activated Slag Cements. *Appl. Geochem.* **2015**, *61*, 233−247.
(40) Shimoda, K.; Tobu, Y.; Kanehashi, K.; Nemoto, T.; Saito, K. Total Understanding of the Local Structures of an Amorphous Slag: Perspective from Multi-Nuclear (^{29}Si, ^{27}Al, ^{17}O, ^{25}Mg, and ^{43}Ca) Solid-State NMR. *J. Non-Cryst. Solids* **2008**, *354*, 1036−1043.
(41) Wang, S.-D.; Scrivener, K. L. ^{29}Si and ^{27}Al NMR Study of Alkali-Activated Slag. *Cem. Concr. Res.* **2003**, *33*, 769−774.
(42) Walkley, B.; Kashani, A.; Sani, M.-A.; Ngo, T. D.; Mendis, P. Examination of Alkali-Activated Material Nanostructure During Thermal Treatment. *J. Mater. Sci.* **2018**, *53*, 9486−9503.
(43) Richardson, I. G.; Brough, A. R.; Brydson, R.; Groves, G. W.; Dobson, C. M. Location of Aluminum in Substituted Calcium Silicate Hydrate (C-S-H) Gels as Determined by ^{29}Si and ^{27}Al NMR and EELS. *J. Am. Ceram. Soc.* **1993**, *76*, 2285−2288.
(44) Rejmak, P.; Dolado, J. S.; Stott, M. J.; Ayuela, A. ^{29}Si NMR in Cement: A Theoretical Study on Calcium Silicate Hydrates. *J. Phys. Chem. C* **2012**, *116*, 9755−9761.
(45) Engelhardt, G.; Michel, D. *High-Resolution Solid State NMR of Silicates and Zeolites*; Wiley: Chichester, 1987.
(46) Walkley, B.; San Nicolas, R.; Sani, M.-A.; Rees, G. J.; Hanna, J. V.; van Deventer, J. S. J.; Provis, J. L. Phase Evolution of C-(N)-A-S-H/N-A-S-H Gel Blends Investigated Via Alkali-Activation of Synthetic Calcium Aluminosilicate Precursors. *Cem. Concr. Res.* **2016**, *89*, 120−135.
(47) McBrierty, V. J.; Douglass, D. C. Recent Advances in the NMR of Solid Polymers. *J. Polym. Sci., Part D: Macromol. Rev.* **1981**, *16*, 295−366.
(48) Rinaldi, R.; Sacerdoti, M.; Passaglia, E. Strätlingite: Crystal Structure, Chemistry, and a Reexamination of Its Polytpye Vertumnite. *Eur. J. Mineral.* **1990**, *2*, 841−850.
(49) Skibsted, J.; Henderson, E.; Jakobsen, H. J. Characterization of Calcium Aluminate Phases in Cements by ^{27}Al MAS NMR Spectroscopy. *Inorg. Chem.* **1993**, *32*, 1013−1027.
(50) Pardal, X.; Brunet, F.; Charpentier, T.; Pochard, I.; Nonat, A. ^{27}Al and ^{29}Si Solid-State NMR Characterization of Calcium-Aluminosilicate-Hydrate. *Inorg. Chem.* **2012**, *51*, 1827−1836.
(51) Houston, J. R.; Maxwell, R. S.; Carroll, S. A. Transformation of Meta-Stable Calcium Silicate Hydrates to Tobermorite: Reaction Kinetics and Molecular Structure from XRD and NMR Spectroscopy. *Geochem. Trans.* **2009**, *10*, 1−14.
(52) Sun, G. K.; Young, J. F.; Kirkpatrick, R. J. The Role of Al in C−S−H: NMR, XRD, and Compositional Results for Precipitated Samples. *Cem. Concr. Res.* **2006**, *36*, 18−29.
(53) Walkley, B.; Page, S. J.; Rees, G. J.; Provis, J. L.; Hanna, J. V. Nanostructure of CaO-(Na_2O)-Al_2O_3-SiO_2-H_2O Gels Revealed by Multinuclear Solid State Magic Angle Spinning and Multiple Quantum Magic Angle Spinning Nuclear Magnetic Resonance Spectroscopy. *J. Phys. Chem. C* **2020**, *124*, 1681−1694.
(54) Manzano, H.; Dolado, J. S.; Ayuela, A. Aluminum Incorporation to Dreierketten Silicate Chains. *J. Phys. Chem. B* **2009**, *113*, 2832−2839.
(55) Faucon, P.; Delagrave, A.; Richet, C.; Marchand, J. M.; Zanni, H. Aluminum Incorporation in Calcium Silicate Hydrates (C−S−H) Depending on Their Ca/Si Ratio. *J. Phys. Chem. B* **1999**, *103*, 7796−7802.
(56) Vyalikh, A.; Massiot, D.; Scheler, U. Structural Characterisation of Aluminium Layered Double Hydroxides by ^{27}Al Solid-State NMR. *Solid State Nucl. Magn. Reson.* **2009**, *36*, 19−23.
(57) Bonk, F.; Schneider, J.; Cincotto, M. A.; Panepucci, H. Characterization by Multinuclear High-Resolution NMR of Hydration Products in Activated Blast-Furnace Slag Pastes. *J. Am. Ceram. Soc.* **2003**, *86*, 1712−1719.
(58) Wang, S.-D.; Scrivener, K. L. Hydration Products of Alkali-Activated Slag Cement. *Cem. Concr. Res.* **1995**, *25*, 561−571.
(59) Kunhi Mohamed, A.; Moutzouri, P.; Berruyer, P.; Walder, B. J.; Siramanont, J.; Harris, M.; Negroni, M.; Galmarini, S. C.; Parker, S. C.; Scrivener, K. L.; Emsley, L.; Bowen, P. The Atomic-Level Structure of Cementitious Calcium Aluminate Silicate Hydrate. *J. Am. Chem. Soc.* **2020**, *142*, 11060−11071.

https://doi.org/10.1021/acs.jpcc.1c07328
J. Phys. Chem. C 2021, 125, 20727−20739